Double diffusive effects on pressure-driven miscible displacement flows in a channel

Manoranjan Mishra, A. De Wit and Kirti Chandra Sahu

Journal of Fluid Mechanics / Volume 712 / December 2012, pp 579 - 597
DOI: 10.1017/jfm.2012.439, Published online:

J. Fluid Mech. (2012), *vol.* 712, *pp.* 579–597.
doi:10.1017/jfm.2012.439

Double diffusive effects on pressure-driven miscible displacement flows in a channel

Manoranjan Mishra[1], **A. De Wit**[2] **and Kirti Chandra Sahu**[3]†

[1] Department of Mathematics, Indian Institute of Technology Ropar, Rupnagar 140 001, Punjab, India

[2] Nonlinear Physical Chemistry Unit, Service de Chimie Physique et Biologie Théorique, Faculté des Sciences, Université Libre de Bruxelles (ULB), CP231, 1050 Brussels, Belgium

[3] Department of Chemical Engineering, Indian Institute of Technology Hyderabad, Yeddumailaram 502 205, Andhra Pradesh, India

(Received 16 November 2011; revised 27 June 2012; accepted 4 September 2012; first published online 9 October 2012)

The pressure-driven miscible displacement of a less viscous fluid by a more viscous one in a horizontal channel is studied. This is a classically stable system if the more viscous solution is the displacing one. However, we show by numerical simulations based on the finite-volume approach that, in this system, double diffusive effects can be destabilizing. Such effects can appear if the fluid consists of a solvent containing two solutes both influencing the viscosity of the solution and diffusing at different rates. The continuity and Navier–Stokes equations coupled to two convection–diffusion equations for the evolution of the solute concentrations are solved. The viscosity is assumed to depend on the concentrations of both solutes, while density contrast is neglected. The results demonstrate the development of various instability patterns of the miscible 'interface' separating the fluids provided the two solutes diffuse at different rates. The intensity of the instability increases when increasing the diffusivity ratio between the faster-diffusing and the slower-diffusing solutes. This brings about fluid mixing and accelerates the displacement of the fluid originally filling the channel. The effects of varying dimensionless parameters, such as the Reynolds number and Schmidt number, on the development of the 'interfacial' instability pattern are also studied. The double diffusive instability appears after the moment when the invading fluid penetrates inside the channel. This is attributed to the presence of inertia in the problem.

Key words: convection, double diffusive convection, fingering instability, interfacial flows (free surface), multiphase and particle-laden flows, multiphase flow

1. Introduction

The dynamics of interface patterns and mixing between two miscible fluids is an active research area (Rashidnia, Balasubramaniam & Schroer 2004; Balasubramaniam *et al.* 2005) and is of importance in many industrial processes, e.g. in enhanced oil recovery, fixed bed regeneration, hydrology and filtration. There exist other industrial applications in which the displacement of one fluid by another miscible/immiscible fluid (Joseph *et al.* 1997) occurs, e.g. in the oil and gas industry, the transportation of crude oil in pipelines relies on the stability of two-layer flows when the highly

† Email address for correspondence: kirtisahu1@gmail.com

viscous fluid is at the wall. In the food processing industries cleaning involves the removal of a highly viscous fluid by water. The stability of this type of two-phase flow in a channel or pipe has been widely investigated both theoretically (Ranganathan & Govindarajan 2001; Selvam *et al.* 2007; Sahu *et al.* 2009*a*; Sahu & Matar 2010, 2011) and experimentally (Hickox 1971; Hu & Joseph 1989; Joseph & Renardy 1992; Joseph *et al.* 1997).

Linear stability analyses of displacement flows in porous media (Saffman & Taylor 1958; Chouke, Van Meurs & Van Der Pol 1959; Tan & Homsy 1986) explain that, if the displacing fluid is less viscous than the displaced one, the interface separating them becomes unstable and a fingering pattern develops at the interface. A review on such dynamics in porous media and Hele-Shaw cells is given by Homsy (1987). In a pipe flow, when a less viscous miscible fluid displaces a more viscous one, a two-layer core–annular flow is obtained in most of the channel/pipe as the elongated 'finger' of the less viscous fluid penetrates into the bulk of the more viscous one. The interface between the two fluids becomes unstable, forming Kelvin–Helmholtz (KH) instabilities and 'roll-up' structures (Joseph *et al.* 1997; Sahu *et al.* 2009*a*,*b*). Experimental studies in miscible core–annular flows (Taylor 1961; Cox 1962; Chen & Meiburg 1996; Petitjeans & Maxworthy 1996; Kuang, Maxworthy & Petitjeans 2003) have focused on analysing the thickness of the more viscous fluid layer left on the pipe walls and the speed of the propagating 'finger' tip. The development of different instability patterns, like axisymmetric 'corkscrew' patterns, in miscible flows has also been investigated (Lajeunesse *et al.* 1997, 1999; Scoffoni, Lajeunesse & Homsy 2001; Cao *et al.* 2003; Gabard & Hulin 2003). Axisymmetric 'pearl' and 'mushroom' patterns were observed in neutrally buoyant core–annular horizontal pipe flows at high Schmidt number and Reynolds number in the range $2 < Re < 60$ (d'Olce *et al.* 2008). By an asymptotic analysis, Yang & Yortsos (1997) studied miscible displacement flows (in Stokes flow regime) between parallel plates and in cylindrical capillaries with large aspect ratio. They found viscous fingering instability for large viscosity ratio and that the displacement efficiency decreases with increasing viscosity ratio.

Goyal, Pichler & Meiburg (2007) performed a linear stability analysis of a miscible displacement flow in a vertical Hele-Shaw cell with a less viscous fluid displacing a more viscous one. They found that the flow develops as a result of linear instability. Their nonlinear simulations of the Stokes equations predict that increasing the unstable density stratification and decreasing diffusion increase the front velocity. The flow fields obtained by these simulations are qualitatively similar to those observed in the experiment of Petitjeans & Maxworthy (1996) in capillary tubes and in the theoretical predictions of Lajeunesse *et al.* (1999) for Hele-Shaw cells. The study of Petitjeans & Maxworthy (1996) discussed the formation and propagation of a single finger for a miscible fluid in a capillary tube. Such dynamics was also found by Taylor (1961) for immiscible fluids.

Thus from the literature discussed above, it has been understood that a hydrodynamic instability of fingering or a KH pattern occur only if the viscosity or density increases along the direction of propagation, i.e. when a less viscous/dense fluid displaces a more viscous/dense fluid. The situation of a more viscous fluid displacing a less viscous one is being classically understood as a stable situation. This stable displacement flow in a vertical cylindrical tube of small diameter was experimentally investigated by Rashidnia *et al.* (2004) and Balasubramaniam *et al.* (2005). For downward displacement (with gravity), the 'interface' separating the fluids becomes unstable and exhibits an asymmetric sinuous shape. On the other hand, in

the case of upward displacement (against gravity), a stable diffusive finger of the more viscous fluid penetrating the less viscous one is observed for small displacement speed. At a larger displacement speed, an axisymmetric finger with a needle-shaped spike propagates out from the main finger tip. To the best of our knowledge, these are the only experiments that have discussed the displacement flow in a classically stable system. A similar situation in a porous medium or Hele-Shaw cell has been investigated theoretically (Pritchard 2009; Mishra *et al.* 2010). They found that double diffusive (DD) effects can destabilize the classically stable situation of a more viscous fluid displacing a less viscous one and affect the viscous fingering dynamics. Therefore, it is interesting to understand whether such a concept of destabilization of an otherwise stable situation by differential diffusion effects can also occur in pressure-driven channel flows if the solvent at hand contains two different solutes influencing the viscosity and diffusing at different rates. Recently, Sahu & Govindarajan (2011) found an unstable DD mode in a classically stable system of three-layer pressure-driven channel flow (with highly and less viscous fluids occupying the core and near-wall regions of the channel, respectively) by conducting a linear stability analysis. The convective and absolute nature of this instability is studied by Sahu & Govindarajan (2012). They assumed that the flow is symmetrical about the channel centreline.

In this context, the main objective of this present study is to understand the influence on the dynamics of differential diffusion between two solutes influencing viscosity when a highly viscous solution of these solutes displaces a less viscous one in a channel without the gravitational force (classically stable system). The two solutions are miscible and their viscosity is a function of the concentration of the two solutes, which diffuse at different rates. The flow dynamics is governed by the continuity and Navier–Stokes equations coupled to two convection–diffusion equations for the concentration of both solutes through a concentration-dependent viscosity. We conduct numerical simulations and analyse destabilization of the flow by differential diffusion effects occurring if the two solutes controlling the viscosity diffuse at different rates. The effects of varying the dimensionless parameters, such as Reynolds number, Schmidt number and ratio of the diffusivity of the species, on the development of interfacial instability patterns are studied. The fundamental challenge in the modelling of the flow configuration addressed here is to consider the Navier–Stokes equation for fluid flow in a channel geometry instead of considering Stokes equations in a capillary tube or Darcy's law in Hele-Shaw geometry.

The rest of this paper is organized as follows. The problem is formulated in § 2, the method of solution using a finite-volume approach is explained in § 3 and the results of the numerical simulations are presented in § 4. Concluding remarks are provided in § 5.

2. Mathematical formulation

Consider a two-dimensional channel initially filled with a stationary Newtonian incompressible fluid containing scalars S and F in quantity S_2 and F_2 and of viscosity μ_2. This solution is displaced by the same solvent in which the scalars are present with different values S_1 and F_1 giving a viscosity μ_1 (see figure 1). The inlet fluid is injected with an average velocity V ($\equiv Q/H$), where Q and H denote the total flow rate and the height of the channel, respectively. We use a rectangular coordinate system (x, y) to model the flow dynamics, where x and y denote the horizontal and

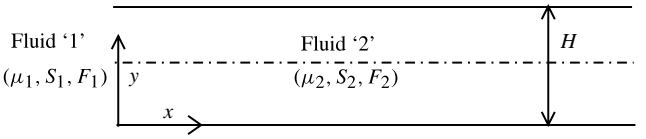

FIGURE 1. Schematic diagram showing the initial flow configuration: fluid '2' occupies the entire channel and is about to be displaced by fluid '1'.

vertical coordinates, respectively. The channel inlet and outlet are located at $x = 0$ and L, respectively. The rigid and impermeable walls of the channel are located at $y = 0$ and H.

In order to determine the flow dynamics, we consider the incompressible Navier–Stokes equations along with the convection–diffusion equations for the conservation of both solutes. The governing equations are given by

$$\boldsymbol{\nabla} \cdot \boldsymbol{u} = 0, \tag{2.1}$$

$$\rho \left[\frac{\partial \boldsymbol{u}}{\partial t} + \boldsymbol{u} \cdot \boldsymbol{\nabla} \boldsymbol{u} \right] = -\boldsymbol{\nabla} p + \boldsymbol{\nabla} \cdot [\mu(\boldsymbol{\nabla} \boldsymbol{u} + \boldsymbol{\nabla} \boldsymbol{u}^{\mathrm{T}})], \tag{2.2}$$

$$\frac{\partial S}{\partial t} + \boldsymbol{u} \cdot \boldsymbol{\nabla} S = \mathscr{D}_s \nabla^2 S, \tag{2.3}$$

$$\frac{\partial F}{\partial t} + \boldsymbol{u} \cdot \boldsymbol{\nabla} F = \mathscr{D}_f \nabla^2 F, \tag{2.4}$$

where $\boldsymbol{u} \equiv (u, v)$ is the velocity vector with components u and v in the x and y directions, respectively, p denotes pressure, and S and F are two scalars with diffusion coefficients $\mathscr{D}_s$ and $\mathscr{D}_f$, respectively, such that $\mathscr{D}_f > \mathscr{D}_s$. The density ρ is taken to be constant. In order to keep the model as simple as possible, the effects of cross-diffusion and of possible dependence of diffusion on concentration are neglected here.

We assume that the viscosity μ has the following dependence on S and F (Mishra *et al.* 2010; Sahu & Govindarajan 2011):

$$\mu = \mu_1 \exp\left[R_s \left(\frac{S - S_1}{S_2 - S_1} \right) + R_f \left(\frac{F - F_1}{F_2 - F_1} \right) \right], \tag{2.5}$$

where $R_s \equiv (S_2 - S_1)\, \mathrm{d}(\ln \mu)/\mathrm{d}S$ and $R_f \equiv (F_2 - F_1)\, \mathrm{d}(\ln \mu)/\mathrm{d}F$ are the log-mobility ratios of solutes S and F, respectively. While there is no experimental evidence in support of (2.5) in a ternary system, it has been widely used to study viscosity-related instabilities (e.g. Chen & Meiburg 1996; Tan & Homsy 1986; Mishra *et al.* 2010), and will be used here for mathematical convenience, and to allow for comparison with previous theoretical work using the same assumption. Since diffusivity and viscosity in a liquid are related approximately inversely through the Stokes–Einstein equation (Probstein 1994), one cannot conduct an experiment in which viscosity varies significantly and diffusivity does not. However, in order to avoid discouraging complexity of the problem right away and in order to build upon previous works, we start here by assuming the diffusion coefficients to be constant.

The following scaling is employed to non-dimensionalize equations (2.1)–(2.5)

$$(x, y) = H(\tilde{x}, \tilde{y}), \quad t = \frac{H^2}{Q}\tilde{t}, \quad (u, v) = \frac{Q}{H}(\tilde{u}, \tilde{v}), \quad p = \frac{\rho Q^2}{H^2}\tilde{p},$$
$$\mu = \tilde{\mu}\mu_1, \quad \tilde{s} = \frac{S - S_1}{S_2 - S_1}, \quad \tilde{f} = \frac{F - F_1}{F_2 - F_1}, \tag{2.6}$$

where the tildes designate dimensionless quantities. After dropping tildes, the dimensionless governing equations become

$$\boldsymbol{\nabla} \cdot \boldsymbol{u} = 0, \tag{2.7}$$

$$\left[\frac{\partial \boldsymbol{u}}{\partial t} + \boldsymbol{u} \cdot \boldsymbol{\nabla}\boldsymbol{u}\right] = -\boldsymbol{\nabla} p + \frac{1}{Re}\boldsymbol{\nabla} \cdot [\mu(\boldsymbol{\nabla}\boldsymbol{u} + \boldsymbol{\nabla}\boldsymbol{u}^{\mathrm{T}})], \tag{2.8}$$

$$\frac{\partial s}{\partial t} + \boldsymbol{u} \cdot \boldsymbol{\nabla} s = \frac{1}{Re\, Sc_s}\nabla^2 s, \tag{2.9}$$

$$\frac{\partial f}{\partial t} + \boldsymbol{u} \cdot \boldsymbol{\nabla} f = \frac{1}{Re\, Sc_f}\nabla^2 f, \tag{2.10}$$

where $Re \equiv \rho Q/\mu_1$, $Sc_s \equiv \mu_1/\rho\mathscr{D}_s$ and $Sc_f \equiv \mu_1/\rho\mathscr{D}_f$ denote the Reynolds number and the Schmidt numbers of the slower- and faster-diffusing solutes, respectively, and $\delta \equiv \mathscr{D}_f/\mathscr{D}_s > 1$ is the ratio of the diffusion coefficients of the faster- and slower-diffusing solutes. Thus $Sc_f = Sc_s/\delta$. The dimensionless viscosity has the following dependence on f and s:

$$\mu = \exp(R_s s + R_f f). \tag{2.11}$$

The initial conditions for s and f in the dimensionless form are $s = f = 0$ everywhere inside the channel and $s = f = 1$ at the inlet. The numerical procedure and boundary conditions used to solve equations (2.7)–(2.10) are described in § 3. Note that, for the boundary conditions used here, when one of the log mobility ratios (either R_f or R_s) is set to zero or $\delta = 1$, the above equations (2.7)–(2.11) reduce to a single solute model, the flow dynamics of which has been discussed using a Navier–Stokes solver by Sahu *et al.* (2009*a*). To have an idea of the order of magnitude of the log mobility ratios for real systems, we note that, if, for instance, the invading fluid is methanol (kinematic viscosity $\nu = 0.6704$ cSt) and the displaced fluid is a mixture of ethylene glycol, acetone and methanol ($\nu = 0.5472$ cSt) (Kalidas & Laddha 1964), we get $R_s = 3$ and $R_f = -3.24$. The values of the parameters will thus be chosen in this order of magnitude.

3. Numerical solution

3.1. *Methods*

We use a finite-volume approach similar to the one developed by Ding, Spelt & Shu (2007) in order to solve the system of equations (2.7)–(2.10). These equations are discretized using a staggered grid. The scalar variables (the pressure and concentrations of the solutes) are defined at the centre of each cell and the velocity components are defined at the cell faces. The discretized convection–diffusion

equations for the conservation of both solutes are given by

$$\frac{\frac{3}{2}s^{n+1} - 2s^n + \frac{1}{2}s^{n-1}}{\Delta t} = \frac{1}{Re\,Sc_s}\nabla^2 s^{n+1} - 2\nabla\cdot(\boldsymbol{u}^n s^n) + \nabla\cdot(\boldsymbol{u}^{n-1}s^{n-1}), \tag{3.1}$$

$$\frac{\frac{3}{2}f^{n+1} - 2f^n + \frac{1}{2}f^{n-1}}{\Delta t} = \frac{1}{Re\,Sc_f}\nabla^2 f^{n+1} - 2\nabla\cdot(\boldsymbol{u}^n f^n) + \nabla\cdot(\boldsymbol{u}^{n-1}f^{n-1}), \tag{3.2}$$

where $\Delta t = t^{n+1} - t^n$ and the superscript n signifies the discretized nth step. In order to discretize the advective terms, i.e the nonlinear terms in (2.9) and (2.10), a weighted essentially non-oscillatory (WENO) scheme is used. A central difference scheme is used to discretize the diffusive term on the right-hand sides of (2.9) and (2.10).

In order to achieve second-order accuracy in the temporal discretization, the Adams–Bashforth and Crank–Nicolson methods are used for the advective and second-order dissipation terms, respectively, in (2.8). This results in the following discretized equation:

$$\frac{\boldsymbol{u}^* - \boldsymbol{u}^n}{\Delta t} = \frac{1}{p^{n+1/2}}\left\{-\left[\frac{3}{2}\mathscr{H}(\boldsymbol{u}^n) - \frac{1}{2}\mathscr{H}(\boldsymbol{u}^{n-1})\right] + \frac{1}{2Re}[\mathscr{L}(\boldsymbol{u}^*, \mu^{n+1}) + \mathscr{L}(\boldsymbol{u}^n, \mu^n)]\right\}, \tag{3.3}$$

where $\boldsymbol{u}^*$ is the intermediate velocity, and $\mathscr{H}$ and $\mathscr{L}$ denote the discrete convection and diffusion operators, respectively. The intermediate velocity $\boldsymbol{u}^*$ is then corrected to the $(n+1)$th time level,

$$\frac{\boldsymbol{u}^{n+1} - \boldsymbol{u}^*}{\Delta t} = \nabla p^{n+1/2}. \tag{3.4}$$

The pressure distribution is obtained from the continuity equation at time step $n+1$ using

$$\nabla\cdot(\nabla p^{n+1/2}) = \frac{\nabla\cdot\boldsymbol{u}^*}{\Delta t}. \tag{3.5}$$

Solutions of the above discretized equations are subject to no-slip, no-penetration and no-flux conditions at the top and bottom walls. A fully developed velocity profile with a constant flow rate taken to be unity is imposed at the inlet ($x = 0$), and Neumann boundary conditions are used at the outlet ($x = L$).

The following steps are employed in our numerical solver in order to solve equations (2.7)–(2.10).

(i) The concentration fields of the solutes are first updated by solving (2.9) and (2.10) with the velocity field at time steps n and $n-1$.

(ii) These are then updated to time step $n+1$ by solving (2.8) together with the continuity equation (2.7).

The numerical procedure described above was developed by Ding *et al.* (2007) in the context of interfacial flows. Sahu *et al.* (2009*a*,*b*) modified this finite-volume method to simulate pressure-driven neutrally buoyant miscible channel flow with high viscosity contrast.

3.2. *Validations*

An important aspect of numerical methods is to choose the optimum grid size for the numerical simulations to obtain the results in considerably less computational

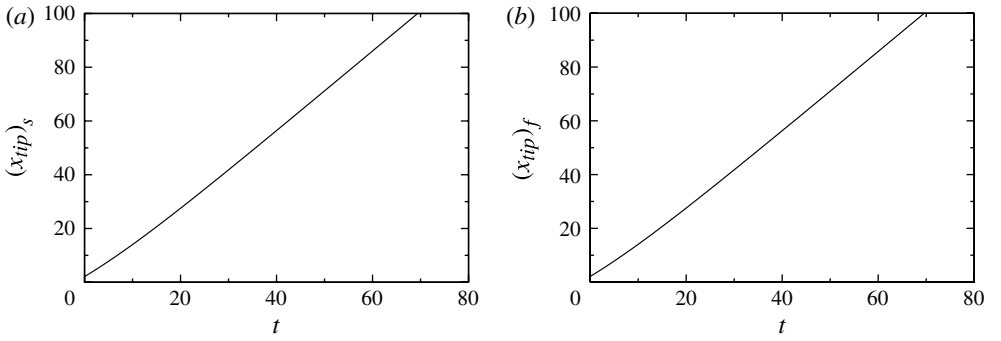

FIGURE 2. Temporal evolution of the position x_{tip} of the leading front separating the two solutions for (*a*) *s* and (*b*) *f* obtained using 81 × 2501 grid points for $Re = 500$, $Sc_s = 20$, $R_s = 3$, $R_f = -3.6$ and $\delta = 5$.

time. It is essential to perform the numerical simulations with different grid points in order to carry out mesh refinement tests and to show convergence of the method. The temporal variations of the spatial location of the leading front separating the two fluids, (x_{tip}), of both solutes *s* and *f* are plotted in figure 2(*a*,*b*), respectively. The parameter values chosen are $Re = 500$, $Sc_s = 20$, $R_s = 3$, $R_f = -3.6$ and $\delta = 5$ in order to incorporate DD phenomena in the simulation. The results are obtained using 81 × 2501 grid points in a channel of aspect ratio 1 : 100. Numerical simulations using 61 × 2001 and 51 × 1601 grids are also conducted in the same computational domain. We found (not shown) that the results are graphically indistinguishable, with a maximum absolute error less than 0.05 %. On the basis of the spatial variation of x_{tip}, one could measure the speed of the finger tip and study the interfacial dynamics (Sahu *et al.* 2009*a*,*b*). It can be seen that the velocity of the leading front between the two solutions is constant, as $(x_{tip})_s$ and $(x_{tip})_f$ both vary linearly with time. The rest of the computations in this paper are performed using 61 × 2001 grid points, in a channel of aspect ratio 1 : 100.

As discussed before, setting $R_f = 0$ (without DD effects), the present governing equations match those given in Sahu *et al.* (2010). Thus, to further validate our code, we reproduced a result of Sahu *et al.* (2010) by studying the spatio-temporal evolution of the concentration of the solute *s* in figure 3. The parameter values are $Re = 500$, $Sc_s = 100$, $R_s = 2.3026$ and $R_f = 0$. Note that $R_s = 2.3026$ corresponds to the unstable case of a less viscous fluid injected into a more viscous one with a viscosity ratio 10 as considered by Sahu *et al.* (2010). It can be seen in figure 3 that the 'interface' becomes unstable, which in turn forms vortical structures and gives rise to intense mixing of the two solutions. During this initial period the flow dynamics is dominated by the formation of KH-type instabilities. At later time ($t > 25$, for this set of parameters) the remnants of *s* assume the form of thin layers adjacent to the upper and lower walls. The flow at this stage is dominated by diffusion.

4. Results and discussion

Let us now analyse the role of differential diffusion on the dynamics and, in particular, investigate how such DD effects can destabilize an otherwise stable situation.

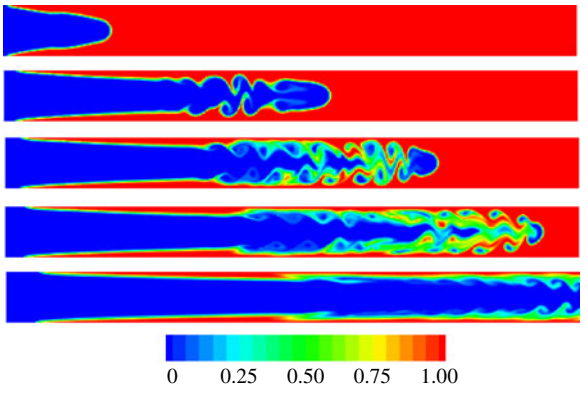

FIGURE 3. (Colour online) Spatio-temporal evolution of the concentration field of solute s at successive times (from top to bottom, $t = 5$, 15, 20, 25 and 40). The rest of the parameter values are $Re = 500$, $Sc_s = 100$, $R_s = 2.3026$ and $R_f = 0$. These results are in excellent agreement with figure 3 of Sahu, Ding & Matar (2010). The greyscale/colour map of all the plots is shown at the bottom.

4.1. *Effects of* δ

The spatio-temporal evolution of the concentration field of solute s for the parameter values $Re = 100$, $Sc_s = 100$, $R_s = 3$ and $R_f = -3.6$ are plotted in figure 4 for different values of δ. In the starting configuration at $t = 0$, the chosen log mobility ratios correspond to a monotonically decreasing viscosity profile at the miscible interface of both fluids, which represents a classically stable interface. For $\delta = 1$ (when $D_f = D_s$), it can be seen that the highly viscous fluid initially displaces the less viscous one like a miscible plug flow and then a fully developed Poiseuille flow regime arises with a pure diffusive miscible interface. Such a stable pattern is termed here as a 'pure–Poiseuille–diffusive' finger (see figure 4*a*). For $\delta > 1$ the miscible interface becomes unstable due to the DD mechanism. Figure 4(*b*) for $\delta = 5$ shows the development of a spike at the tip of the finger and the fact that the miscible interface deviates from the 'pure–Poiseuille–diffusive' finger. For a larger δ (see figure 4*c* for $\delta = 10$), the flow becomes unstable, forming symmetrical wavy interfaces because of a KH-type instability. At later stages the flow dynamics is like a three-layer core–annular flow (Chen & Meiburg 1996; Petitjeans & Maxworthy 1996; Kuang *et al.* 2003). These instabilities occur at the interface primarily because a viscosity contrast arises due to the DD effects. At the tip of the single finger a 'cap-type' instability is observed for the large value of $\delta = 10$ (see figure 4*c*) unlike the spike-like instability for the moderate value of $\delta = 5$ (figure 4*b*). This 'cap-type' instability leads to a mushroom structure at very late times.

In order to investigate the mechanism of the instability for $\delta > 1$, the viscosity fields for the parameter values of figure 4 are plotted in figure 5. It is seen that, at the wall, a highly viscous stenosis region is formed due to the DD effects when $\delta > 1$. Such a region does not occur if $\delta = 1$. This viscous stenosis region increases with increasing δ. A highly viscous region behind the wall was also observed in the miscible displacement experiment of Taylor (1961). In figure 5(*a*), which corresponds to $\delta = 1$, a viscosity profile decreasing monotonically along the axial direction is obtained at any fixed transverse axis. But for $\delta > 1$ the viscosity profile becomes non-monotonic in the axial direction and features locally a less viscous fluid layer

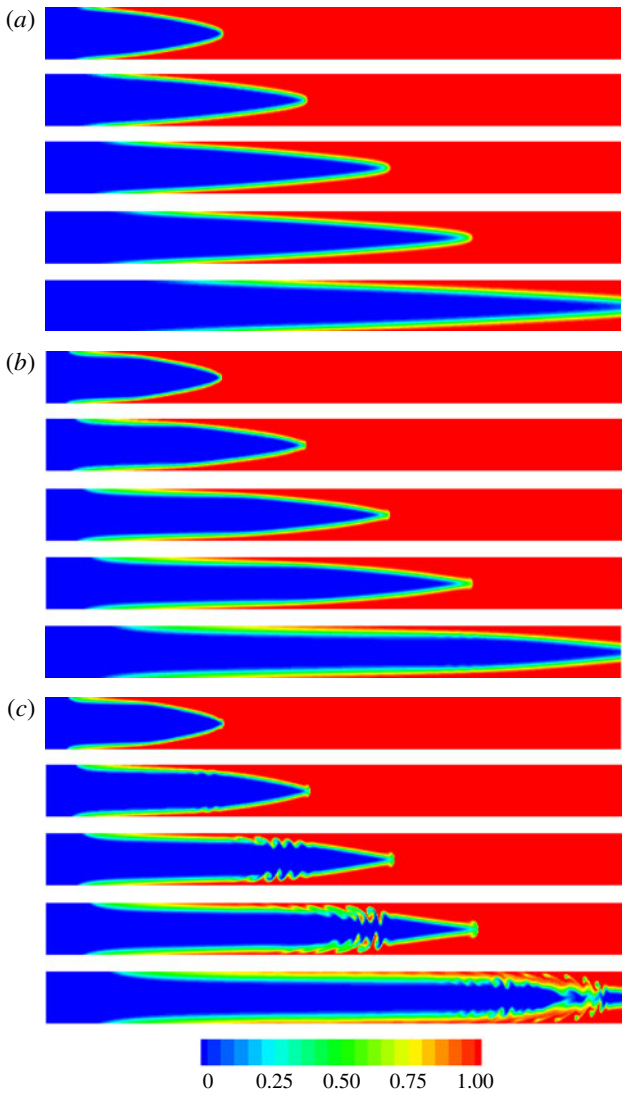

FIGURE 4. (Colour online) Spatio-temporal evolution of the concentration field of solute s at successive times (from top to bottom, $t = 20$, 30, 40, 50 and $t = 75$) for (a) $\delta = 1$, (b) $\delta = 5$ and (c) $\delta = 10$. The rest of the parameter values are $Re = 100$, $Sc_s = 100$, $R_s = 3$ and $R_f = -3.6$.

between two more viscous layers (see figure 5 for $\delta = 5$). This is similar to the situation in DD viscous fingering in porous media (Mishra *et al.* 2010). For $\delta = 10$, rolling structures similar to those in the contours of s (in figure 4) are also observed in the viscosity contours shown in figure 5(c).

We further analyse the spatial distribution of viscosity by plotting in figure 6 the evolution in time of the axial variation of the transverse averaged viscosity, $\overline{\mu} = \int_0^1 \mu \, \mathrm{d}y$. It can be seen in figure 6(a) that $\overline{\mu}$ varies monotonically in the axial direction for $\delta = 1$. The variation of $\overline{\mu}$ is however non-monotonic for $\delta = 5$ and 10. Hence, a local maximum develops such that, locally, the less viscous zone close to

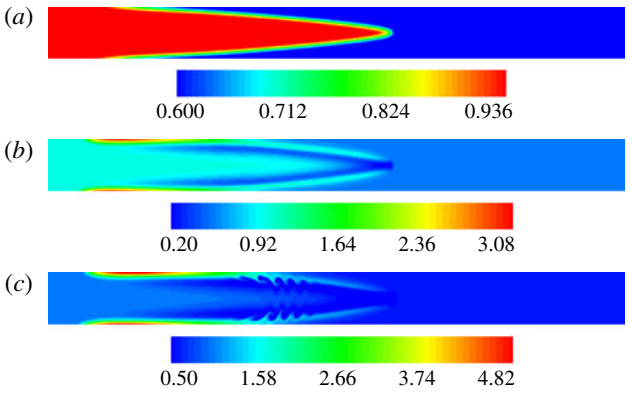

FIGURE 5. (Colour online) The viscosity field at $t = 40$ for (a) $\delta = 1$, (b) $\delta = 5$ and (c) $\delta = 10$ and the simulations of figure 4.

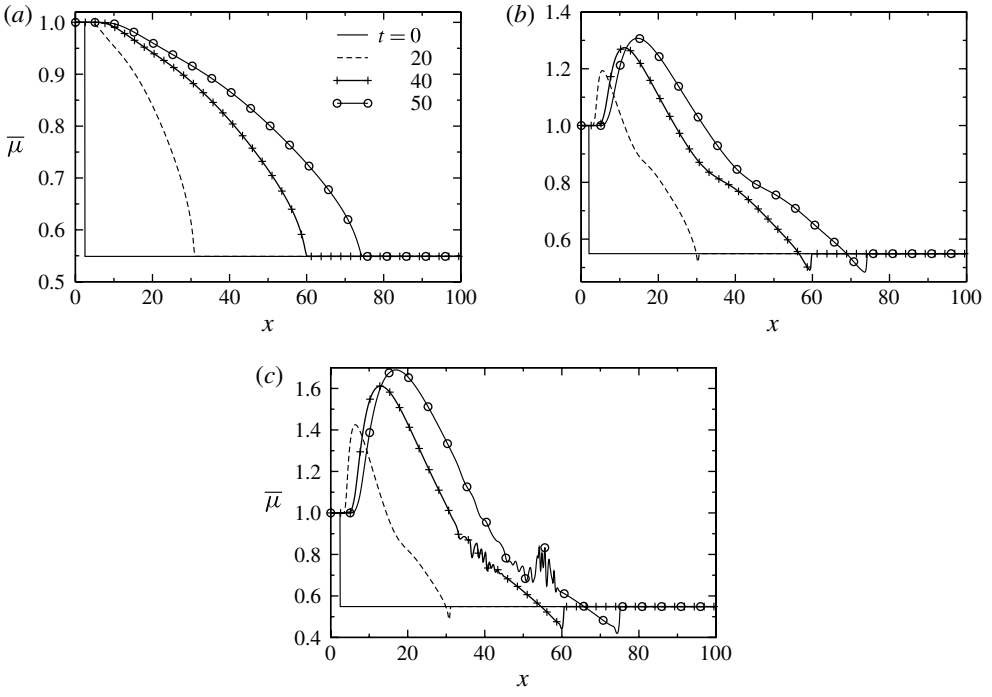

FIGURE 6. Variation of transverse average viscosity $\overline{\mu} = \int_0^1 \mu \, dy$ in the streamwise direction for (a) $\delta = 1$, (b) $\delta = 5$ and (c) $\delta = 10$ and parameters of figure 4.

the injection side displaces a more viscous region. This is the main cause of the instabilities that can occur in pressure-driven displacement flows of a less viscous fluid by a more viscous one in a channel, as studied here. This non-monotonic character of the viscosity profile due to DD effects was also found in viscous fingering of the classically stable displacement of a less viscous fluid by a more viscous one in porous media (Mishra *et al.* 2010). At early times, the instability starts here at the axial

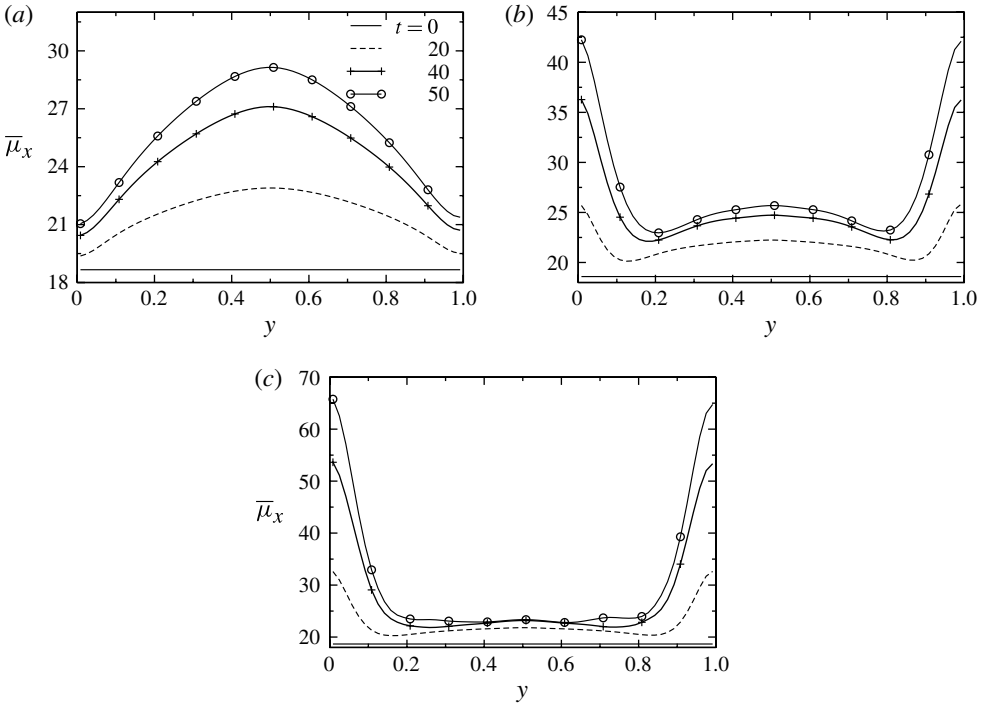

FIGURE 7. Variation of axially averaged viscosity $\overline{\mu}_x = \int_0^{L/H} \mu \, \mathrm{d}x$ in the streamwise direction for (*a*) $\delta = 1$, (*b*) $\delta = 5$ and (*c*) $\delta = 10$ and parameters of figure 4.

station (after the viscous stenosis region) where there is a change in the slope of the viscosity curve. The spike/cap instability occurs at the tip of the single finger where $\overline{\mu}$ decreases to a value smaller than the initial viscosity at that location (figure 6*b*,*c*). For $\delta = 10$, the KH instability occurs approximately in the region $(35 < x < 60)$ at $t = 40$ where there is a large zig-zag oscillation in $\overline{\mu}$. The length of this region increases with time (see figure 6*c*).

In figure 7, we plot the evolution of the transverse variation of the axially averaged viscosity, $\overline{\mu}_x = \int_0^{L/H} \mu \, \mathrm{d}x$. For $\delta = 1$ it can be seen in figure 7(*a*) that $\overline{\mu}_x$ is maximum at the centreline of the channel. Thus it is similar to a core–annular flow where the less and more viscous fluids occupy the annular and core regions, respectively. This is known to be a stable situation in core–annular types of flow (Sahu & Govindarajan 2011). Unlike for $\delta = 1$, when $\delta = 5$ and 10, the viscosity is maximum near the wall regions, which, in the context of core–annular flow, is an unstable situation, as discussed in Selvam *et al.* (2007) and Sahu & Govindarajan (2011). Close inspection also reveals that increasing δ increases the viscosity near the wall regions, and thus has a destabilizing effect.

During the displacement process, as the highly viscous fluid displaces the less viscous one, the total viscosity inside the channel is expected to increase linearly. This behaviour can be seen for $\delta = 1$ in figure 8, where the normalized total averaged viscosity, $\mu_{av} \equiv (1/\mu_0) \int_0^L \overline{\mu} \, \mathrm{d}x$, is plotted versus time. Here, μ_0 is the total viscosity at $t = 0$, when only the displaced solution (solution '2') is present inside the channel. The dotted line in figure 8 represents the analytical solution for the plug-flow

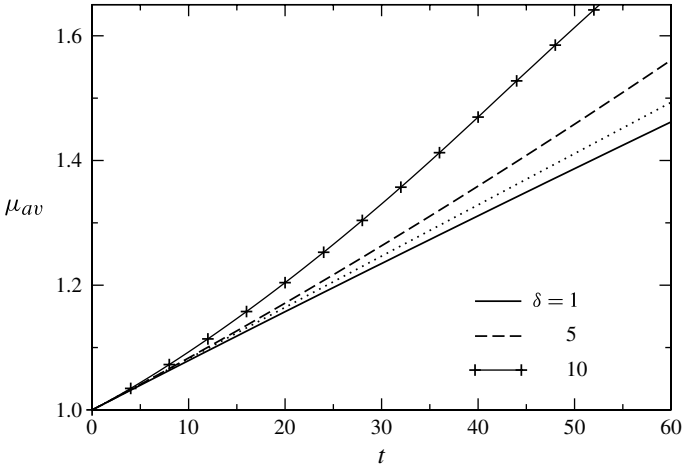

FIGURE 8. Variation of normalized average viscosity $\mu_{av} = (1/\mu_0)\int_0^L \overline{\mu}\,\mathrm{d}x$ with time for different values of δ and parameters of figure 4. The dotted line represents the analytical solution for the plug-flow displacement, given by $\mu_{av} = 1 + (t/L)[\mathrm{e}^{-(R_s+R_f)} - 1]$.

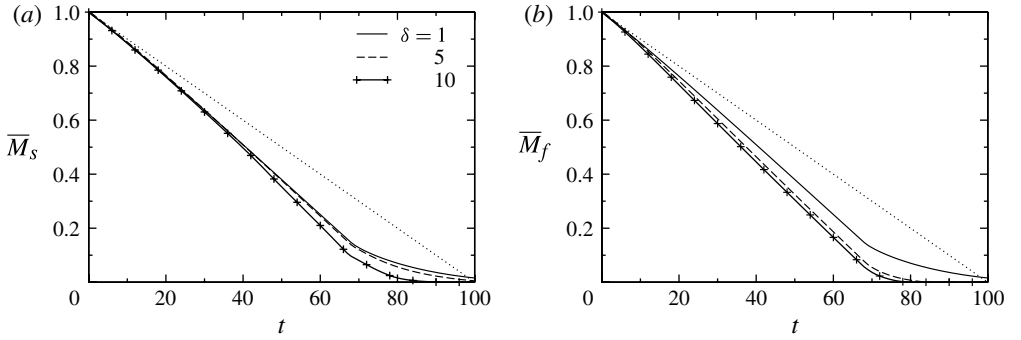

FIGURE 9. Measure of the normalized mass of the displaced fluid: (*a*) $\overline{M}_s = M_{s_{0.98}}/M_{s1}$ of solute '*s*' and (*b*) $\overline{M}_f = M_{f_{0.98}}/M_{f1}$ of solute '*f*', for different values of δ. The dotted lines represent the analytical solution of plug-flow displacement, given by $\overline{M}_s = \overline{M}_f = 1 - tH/L$.

displacement, given by $\mu_{av} = 1 + t[\mathrm{e}^{-(R_s+Rf)} - 1]/L$. It can be seen that, for this set of parameter values, the line corresponding to $\delta = 1$ is close to this analytical solution. For $\delta > 1$, μ_{av} increases at a higher rate than for $\delta = 1$. This rate increases with increasing δ. The rate of increase of viscosity remains the same nearly until the time $t = 5$ for all the δ values considered, which implies that the onset of DD effects in the case of channel flows occurs very early (approximately at $t = 5$ for this set of parameter values). In porous media the DD effects start from the very beginning (Mishra *et al.* 2010). This delay here of the onset of the DD effects is attributed to the presence of inertia in the present problem.

In figure 9(*a*,*b*), we plot the temporal evolution of the normalized mass of the displaced solute s ($\overline{M}_s = M_{s_{0.98}}/M_{s_1}$) and f ($\overline{M}_f = M_{f_{0.98}}/M_{f_1}$), respectively. Here, M_{s_1} and M_{f_1} are the initial masses of the solutes s and f, respectively, and $M_{s_{0.98}}$ and $M_{f_{0.98}}$ are the masses corresponding concentration labels >0.98 of the solutes s and f, respectively. The parameter values are the same as those used to generate figure 4.

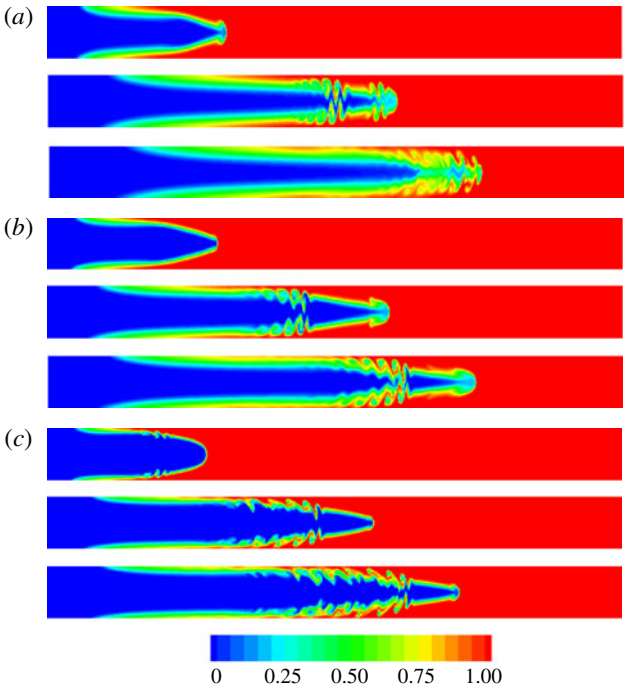

FIGURE 10. (Colour online) Spatio-temporal evolution of the concentration field of solute s at successive times (from top to bottom, $t = 20$, 40 and 50) for (*a*) $Re = 100$, (*b*) $Re = 200$ and (*c*) $Re = 500$. The rest of the parameter values are $\delta = 10$, $Sc_s = 20$, $R_s = 3$ and $R_f = -3.6$.

Inspection of figure 9 reveals that $\overline{M}_s$ and $\overline{M}_f$ undergo an almost linear decrease at the early stages of the flow due to the displacement by solution '1'. The slope of the curve during this linear stage is considerably steeper than that of the line represented by $1 - tH/L$. This corresponds to the plug-flow displacement of solution '2' by solution '1' when the sharp interface separating the two solutions has not yet reached the channel exit. At this early stage, the flow dynamics is dominated by the formation of vortical structures for the larger δ values. As shown in figure 4, the intensity of the instabilities increases with increasing δ. These manifest themselves via the formation of vortical structures, which give rise to intense mixing of the two fluids and a rapid displacement of the solutes present inside the channel. It can be seen in figure 9 that the displacement rate increases with increasing δ. At approximately $t = 70$ for this set of parameters when the 'front' of the displacing fluid '1' reaches the end of the simulation domain, a transition to another linear regime occurs. The slope of the $\overline{M}_s$ and $\overline{M}_f$ versus time plot is much smaller than the previous one. In this regime the flow dynamics is dominated by diffusion. Close inspection of figure 9 also reveals that up to $t = 5$ the slopes of $\overline{M}_s$ and $\overline{M}_f$ versus time are the same for all values of δ, confirming the delay in the onset of DD effects in pressure-driven displacement flows as described in figure 8.

4.2. *Effects of Re and* Sc_s

We have also carried out a parametric study to investigate the effect of varying the Reynolds number on the displacement characteristics for $\delta = 10$, $Sc_s = 20$, $R_s = 3$

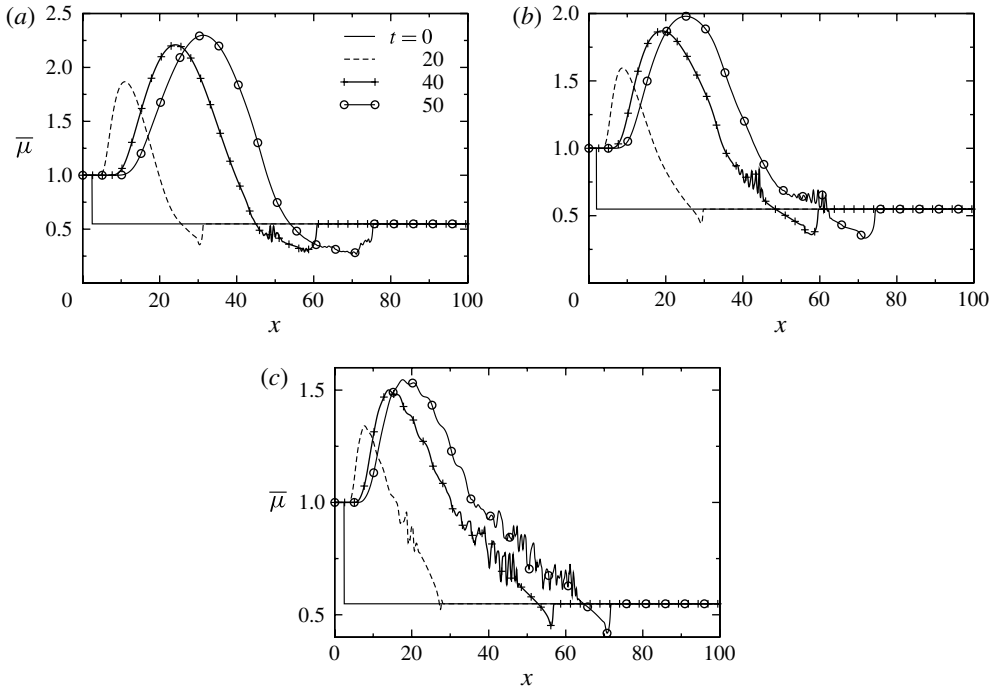

FIGURE 11. Variation of transverse average viscosity, $\overline{\mu}$, in the streamwise direction for (*a*) $Re = 100$, (*b*) $Re = 200$ and (*c*) $Re = 500$ and parameter values of figure 10.

and $R_f = -3.6$. In figure 10, it is seen that increasing the value of Re from 100 to 200 and then to 500, respectively, leads to the rapid development of instabilities that lead to complex dynamics and intricate flow patterns. These are punctuated by more pronounced roll-up phenomena. Note that, for these parameter values, the flow is in a laminar regime. A close inspection of figure 10 also reveals that the diffusive mixing decreases with increasing Re. This is due to the decrease in effective diffusion, characterized by the Péclet number $Pe \equiv Re\, Sc_s$, with increasing Re. It can be seen that a mushroom-like structure appears at the tip of the leading finger. However, it is persistent only for the intermediate value of Re. The decrease in the effective Péclet number (highly diffusive mixing) for the low value $Re = 100$ destroys this structure at the nose of the leading finger. For $Re = 500$ the diffusive mixing is very small and the interface separating the fluids becomes sharper. It can be seen that the location of the appearance of the KH-type instabilities is shifted towards the tip of the finger when decreasing the Reynolds number.

The evolution of the corresponding axial variation of the transverse averaged viscosity $\overline{\mu}$ is plotted for $Re = 100$, 200 and 500 in figure 11. It can be seen that the variation of $\overline{\mu}$ is non-monotonic for all values of Re considered. Here, we study a case with highly diffusive mixing ($Sc_s = 20$), unlike figure 6, which corresponds to $Sc_s = 100$ (low diffusion). However like low diffusive flow, the instability starts near the viscous stenosis region (not shown) in this case too. The mushroom (spike/cap) type instability occurs at the tip of the single finger when $\overline{\mu}$ decreases to a value smaller than the initial viscosity and gradually (suddenly) increases to the initial viscosity (see figure 11). It can be seen that the zig-zag oscillation in $\overline{\mu}$, which corresponds to the KH instability region, moves in the axial direction. The evolution

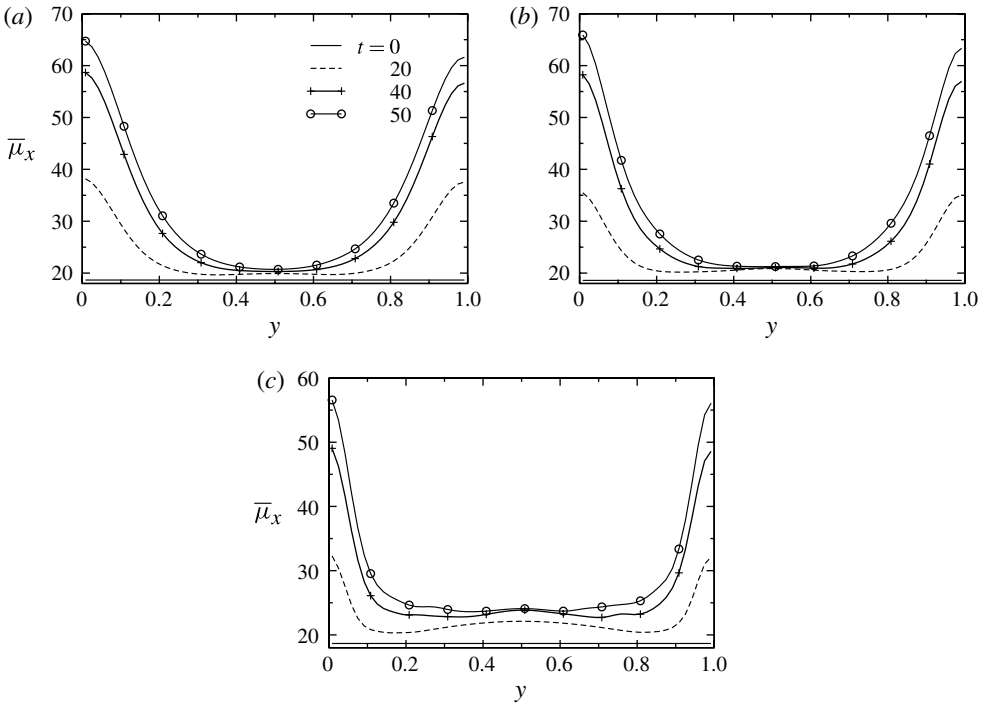

FIGURE 12. Variation of axially averaged viscosity, $\overline{\mu}_x$, in the streamwise direction for (*a*) $Re = 100$, (*b*) $Re = 200$ and (*c*) $Re = 500$ and parameter values of figure 10.

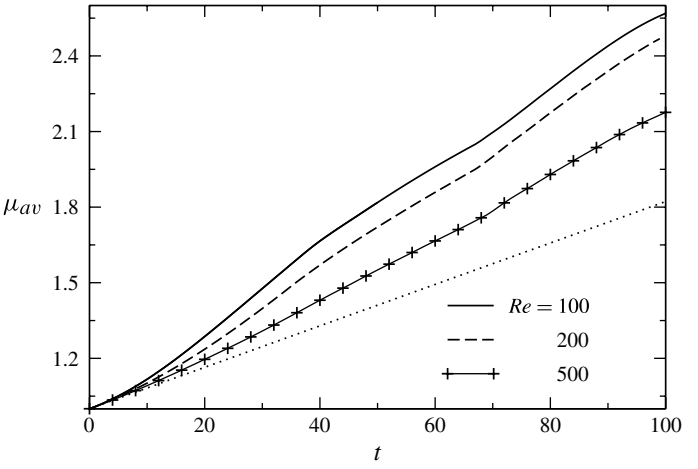

FIGURE 13. Variation of normalized average viscosity, μ_{av}, with time for simulations of figure 10. The dotted line represents the analytical solution for the plug-flow displacement.

of the transverse variation of the axially averaged viscosity, $\overline{\mu}_x$, plotted in figure 12, reveals that, as time progresses, the viscosity near the walls increases and the local maximum of the curve moves towards the channel wall, which in turn destabilizes the flow. The normalized total averaged viscosity, μ_{av} is plotted versus time in figure 13 for different values of *Re*. The dotted line in figure 13 represents the analytical

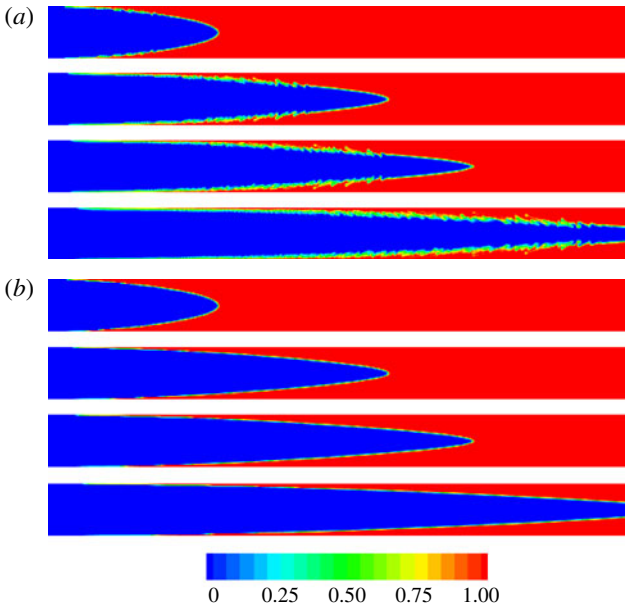

FIGURE 14. (Colour online) Spatio-temporal evolution of the concentration field of solute s at successive times (from top to bottom, $t = 20$, 40, 50, 75 and 95) for (*a*) $Sc_s = 10^3$ and (*b*) $Sc_s = 10^5$. Other parameter values are $\delta = 10$, $Re = 200$, $R_s = 3$ and $R_f = -3.6$.

solution for the plug-flow displacement. It can be seen that μ_{av} increases almost linearly for all values of Re considered. The slope increases with increasing Re and is considerably larger than that of the analytical solution. Close inspection of figure 13 also reveals that these lines overlap up to $t = 5$ (approximately), which confirms the delay in the onset of DD effects as compared to the phenomena observed in porous media.

Finally, we study in figure 14 the flow dynamics for very large Schmidt numbers, i.e. $Sc_s = 10^3$ and 10^5. The rest of the parameter values are $\delta = 10$, $Re = 200$, $R_s = 3$ and $R_f = -3.6$. While instabilities due to DD effects can still be seen for $Sc_s = 10^3$, the flow is stable for $Sc_s = 10^5$. In this case the Schmidt number of the faster-diffusing solute Sc_f is 10^4 for $\delta = 10$. As the Schmidt numbers of both the solutes are quite large (practically in the immiscible limit), the diffusive effects are not destabilizing. This is also evidenced in figure 15, showing that, for $Sc_s = 10^5$, the profiles of the axially averaged viscosity $\overline{\mu}_x$ are qualitatively similar to those of the stable single-component system ($\delta = 1$) shown in figure 7(*a*). However, a close inspection of figure 15(*b*) reveals that, unlike in figure 7(*a*), $\overline{\mu}_x$ smoothly approaches a constant value just near the wall, which is stabilizing the flow.

5. Concluding remarks

Pressure-driven displacements within a horizontal channel of two different solutions of two scalars influencing the viscosity and having different diffusion rates are studied here numerically. We consider specifically the displacement of a less viscous solution, which occupies the channel initially, by a more viscous one. We show that such a classically stable displacement can become unstable if the two solutes impacting the viscosity diffuse at sufficiently different rates. In our simulations, the continuity

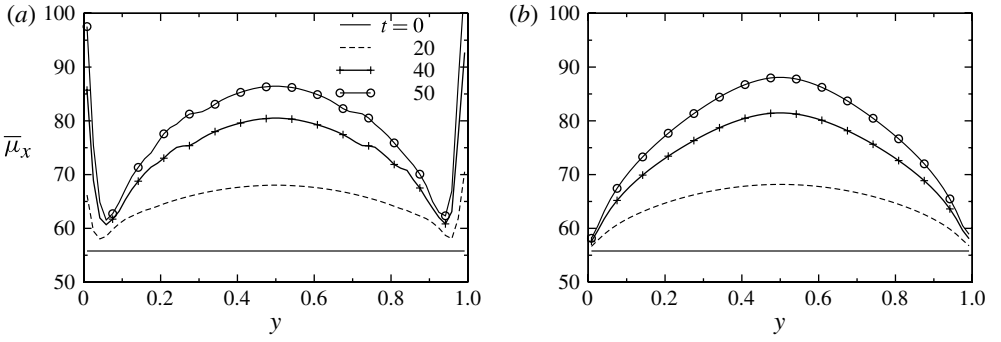

FIGURE 15. Variation of the axially averaged viscosity, $\overline{\mu}_x$, in the streamwise direction for (*a*) $Sc_s = 10^3$ and (*b*) $Sc_s = 10^5$. The rest of the parameter values are as in figure 14.

and Navier–Stokes equations coupled to two convection–diffusion equations for the concentration of both solutes are solved using a finite-volume approach. The viscosity is assumed to be an exponential function of the concentrations of both solutes. In order to isolate the effects of viscosity contrast, the density is assumed to be the same for both the fluids. The numerical code has been validated by conducting a grid-refinement test and also reproducing the results of single-component displacement flow (Sahu & Matar 2010). The results demonstrate the development of various instability patterns of the 'interface' separating the fluids when DD effects are present. The intensity of the instability increases with increasing diffusivity ratio between the faster-diffusing and the slower-diffusing solutes. This instability brings about fluid mixing and accelerates the displacement of the solution originally occupying the channel. The effects of the dimensionless parameters, such as Reynolds number and Schmidt number, on the development of the 'interfacial' instability pattern are also studied. A mushroom-like structure appears at the tip of the leading finger, which is persistent only for intermediate values of *Re*. The DD instability appears after the invading fluid penetrates inside the channel. This is attributed to the presence of inertia in the present problem. These different types of instabilities can be obtained by specifying the slow and fast components as mass and heat typically. Experimentally, the predicted instability can be looked for using two non-reacting chemical species both influencing the viscosity of the solution and having different diffusion coefficients as in the case of two polymers with chains of different length, for instance.

Note that we have here assumed that the diffusion is pseudo-binary and that the diffusion coefficients are constant and do not depend on solute concentration. Further developments could be made to include cross-diffusion or concentration-dependent diffusion (Curtiss & Hirschfelder 1949). Moreover, as mentioned above, the Stokes–Einstein relationship (Probstein 1994) shows that, in a solution, it is not possible that viscosity varies significantly without a correspondingly strong variation in diffusivity. Preliminary computations performed to account for the Stokes–Einstein dependence of diffusivity on viscosity show that, although DD effects still destabilize the system, some feature of the results are qualitatively different. These aspects should be the focus of additional future studies. Eventually, let us note that we have here also used an exponential viscosity–concentration relationship. Other viscosity–concentration models (Iglesias-Silva & Hall 2010) or non-monotonic viscosity profiles (Manickam & Homsy 1993) could be investigated in future studies along the same lines.

Acknowledgements

Grateful thanks are extended to Professor R. Govindarajan for her valuable suggestions. K.S. thanks the Department of Science and Technology and the Indian Institute of Technology Hyderabad, India, for financial support. M.M. acknowledges the financial support from the Department of Science and Technology and the Indian Institute of Technology Ropar, India. A.D. acknowledges FNRS and Prodex for financial support.

REFERENCES

BALASUBRAMANIAM, R., RASHIDNIA, N., MAXWORTHY, T. & KUANG, J. 2005 Instability of miscible interfaces in a cylindrical tube. *Phys. Fluids* **17**, 052103.

CAO, Q., VENTRESCA, L., SREENIVAS, K. R. & PRASAD, A. K. 2003 Instability due to viscosity stratification downstream of a centreline injector. *Can. J. Chem. Engng* **81**, 913.

CHEN, C.-Y. & MEIBURG, E. 1996 Miscible displacement in capillary tubes. Part 2. Numerical simulations. *J. Fluid Mech.* **326**, 57–90.

CHOUKE, R. L., VAN MEURS, P. & VAN DER POL, C. 1959 The instability of slow, immiscible, viscous liquid–liquid displacements in permeable media. *Trans. AIME* **216**, 188.

COX, B. G. 1962 On driving a viscous fluid out of a tube. *J. Fluid Mech.* **14**, 81.

CURTISS, C. F. & HIRSCHFELDER, J. O. 1949 Transport properties of multicomponent gas mixtures. *J. Chem. Phys.* **17**, 550–555.

DING, H., SPELT, P. D. M. & SHU, C. 2007 Diffuse interface model for incompressible two-phase flows with large density ratios. *J. Comput. Phys.* **226**, 2078–2095.

D'OLCE, M., MARTIN, J., RAKOTOMALALA, N., SALIN, D. & TALON, L. 2008 Pearl and mushroom instability patterns in two miscible fluids' core annular flows. *Phys. Fluids* **20**, 024104.

GABARD, C. & HULIN, J.-P. 2003 Miscible displacement of non-Newtonian fluids in a vertical tube. *Eur. Phys. J.* E **11**, 231.

GOYAL, N., PICHLER, H. & MEIBURG, E. 2007 Variable-density miscible displacements in a vertical Hele-Shaw cell: linear stability. *J. Fluid Mech.* **584**, 357–372.

HICKOX, C. E. 1971 Instability due to viscosity and density stratification in axisymmetric pipe flow. *Phys. Fluids* **14**, 251.

HOMSY, G. M. 1987 Viscous fingering in porous media. *Annu. Rev. Fluid Mech.* **19**, 271–311.

HU, H. H. & JOSEPH, D. D. 1989 Lubricated pipelining: stability of core–annular flows. Part 2. *J. Fluid Mech.* **205**, 395.

IGLESIAS-SILVA, G. A. & HALL, K. R. 2010 Equivalence of the McAllister and Heric equations for correlating the liquid viscosity of multicomponent mixtures. *Ind. Engng Chem. Res.* **49**, 6250–6254.

JOSEPH, D. D., BAI, R., CHEN, K. P. & RENARDY, Y. Y. 1997 Core–annular flows. *Annu. Rev. Fluid Mech.* **29**, 65.

JOSEPH, D. D. & RENARDY, Y. Y. 1992 *Fundamentals of Two-Fluid Dynamics. Part II: Lubricated Transport, Drops and Miscible Liquids*. Springer.

KALIDAS, R. & LADDHA, S. 1964 Viscosity of ternary liquid mixtures. *J. Chem. Engng Data* **9**, 142–145.

KUANG, J., MAXWORTHY, T. & PETITJEANS, P. 2003 Miscible displacements between silicone oils in capillary tubes. *Eur. J. Mech.* **22**, 271.

LAJEUNESSE, E., MARTIN, J., RAKOTOMALALA, N. & SALIN, D. 1997 3D instability of miscible displacements in a Hele-Shaw cell. *Phys. Rev. Lett.* **79**, 5254.

LAJEUNESSE, E., MARTIN, J., RAKOTOMALALA, N., SALIN, D. & YORTSOS, Y. C. 1999 Miscible displacement in a Hele-Shaw cell at high rates. *J. Fluid Mech.* **398**, 299.

MANICKAM, O. & HOMSY, G. M. 1993 Stability of miscible displacements in porous media with nonmonotonic viscosity profiles. *Phys. Fluids* **5**, 1356–1367.

MISHRA, M., TREVELYAN, P. M. J., ALMARCHA, C. & DE WIT, A. 2010 Influence of double diffusive effects on miscible viscous fingering. *Phys. Rev. Lett* **105**, 204501.

PETITJEANS, P. & MAXWORTHY, T. 1996 Miscible displacements in capillary tubes. Part 1. Experiments. *J. Fluid Mech.* **326**, 37.

PRITCHARD, D. 2009 The linear stability of double-diffusive miscible rectilinear displacements in a Hele-Shaw cell. *Eur. J. Mech. (*B/*Fluids*) **28** (4), 564–577.

PROBSTEIN, R. F. 1994 *Physicochemical Hydrodynamics*. Wiley.

RANGANATHAN, B. T. & GOVINDARAJAN, R. 2001 Stabilisation and destabilisation of channel flow by location of viscosity-stratified fluid layer. *Phys. Fluids* **13** (1), 1–3.

RASHIDNIA, N., BALASUBRAMANIAM, R. & SCHROER, R. T. 2004 The formation of spikes in the displacement of miscible fluids. *Ann. N.Y. Acad. Sci.* **1027**, 311–316.

SAFFMAN, P. G. & TAYLOR, G. I. 1958 The penetration of a finger into a porous medium in a Hele-Shaw cell containing a more viscous liquid. *Proc. R. Soc. Lond.* A **245**, 312–329.

SAHU, K. C., DING, H. & MATAR, O. K. 2010 Numerical simulation of non-isothermal pressure-driven miscible channel flow with viscous heating. *Chem. Engng Sci.* **65**, 3260–3267.

SAHU, K. C., DING, H., VALLURI, P. & MATAR, O. K. 2009*a* Linear stability analysis and numerical simulation of miscible channel flows. *Phys. Fluids* **21**, 042104.

SAHU, K. C., DING, H., VALLURI, P. & MATAR, O. K. 2009*b* Pressure-driven miscible two-fluid channel flow with density gradients. *Phys. Fluids* **21**, 043603.

SAHU, K. C. & GOVINDARAJAN, R. 2011 Linear stability of double-diffusive two-fluid channel flow. *J. Fluid Mech.* **687**, 529–539.

SAHU, K. C. & GOVINDARAJAN, R. 2012 Spatio-temporal linear stability of double-diffusive two-fluid channel flow. *Phys. Fluids* **24**, 054103.

SAHU, K. C. & MATAR, O. K. 2010 Three-dimensional linear instability in pressure-driven two-layer channel flow of a Newtonian and a Herschel–Bulkley fluid. *Phys. Fluids* **22**, 112103.

SAHU, K. C. & MATAR, O. K. 2011 Three-dimensional convective and absolute instabilities in pressure-driven two-layer channel flow. *Intl J. Multiphase Flow* **37**, 987–993.

SCOFFONI, J., LAJEUNESSE, E. & HOMSY, G. M. 2001 Interface instabilities during displacement of two miscible fluids in a vertical pipe. *Phys. Fluids* **13**, 553.

SELVAM, B., MERK, S., GOVINDARAJAN, R. & MEIBURG, E. 2007 Stability of miscible core–annular flows with viscosity stratification. *J. Fluid Mech.* **592**, 23–49.

TAN, C. T. & HOMSY, G. M. 1986 Stability of miscible displacements: rectilinear flow. *Phys. Fluids* **29**, 73549.

TAYLOR, G. I. 1961 Deposition of viscous fluid on the wall of a tube. *J. Fluid Mech.* **10**, 161.

YANG, Z. & YORTSOS, Y. C. 1997 Asymptotic solutions of miscible displacements in geometries of large aspect ratio. *Phys. Fluids* **9**, 286–298.